Gravity Wave Generation in Balanced Sheared Flow Revisited

MANITA CHOUKSEY,[a] CARSTEN EDEN,[a] AND DIRK OLBERS[c,b]

[a] *Institut für Meereskunde, Universität Hamburg, Hamburg, Germany*
[b] *MARUM, Universität Bremen, Bremen, Germany*
[c] *Alfred Wegener Institut für Polar- und Meeresforschung, Bremerhaven, Germany*

(Manuscript received 31 May 2021, in final form 29 January 2022)

ABSTRACT: The generation of internal gravity waves from an initially geostrophically balanced flow is diagnosed in nonhydrostatic numerical simulations of shear instabilities for varied dynamical regimes. A nonlinear decomposition method up to third order in the Rossby number (Ro) is used as the diagnostic tool for a consistent separation of the balanced and unbalanced motions in the presence of their nonlinear coupling. Wave emission is investigated in an Eady-like and a jet-like flow. For the jet-like case, geostrophic and ageostrophic unstable modes are used to initialize the flow in different simulations. Gravity wave emission is in general very weak over a range of values for Ro. At sufficiently high Ro, however, when the condition for symmetric instability is satisfied with negative values of local potential vorticity, significant wave emission is detected even at the lowest order. This is related to the occurrence of fast ageostrophic instability modes, generating a wide spectrum of waves. Thus, gravity waves are excited from the instability of the balanced mode to lowest order only if the condition of symmetric instability is satisfied and ageostrophic unstable modes obtain finite growth rates.

SIGNIFICANCE STATEMENT: We aim to understand the generation of internal gravity waves in the atmosphere and ocean from a flow field that is initially balanced, i.e., free from any internal gravity waves. To examine this process, we use simulations from idealized numerical models and nonlinear flow decomposition method to identify waves. Our results show that a prominent mechanism by which waves can be generated is related to symmetric or ageostrophic instabilities of the balanced flow possibly occurring during frontogenesis. This process can be a significant mechanism to dissipate the energy of the geostrophic flow in the ocean.

KEYWORDS: Gravity waves; Inertia-gravity waves; Internal waves; Shear structure/flows; Waves, atmospheric; Waves, oceanic

1. Introduction

Gravity wave generation from a balanced flow by internal mechanisms and the importance of spontaneous loss of balance in the atmospheric and oceanic flows still poses open questions. Gravity wave emission seen in observations (e.g., Plougonven and Zhang 2014), laboratory experiments (e.g., Williams et al. 2008), and numerical simulations (e.g., Plougonven and Snyder 2007) is often attributed to spontaneous loss of balance of the balanced flow. However, to correctly associate the generated waves to a particular mechanism, an exact description and diagnosis of balanced flow are important, but this remains theoretically and practically challenging. In this paper, we extend our diagnosis from Eden et al. (2019a) to detect gravity wave emission from an initially balanced shear flow using higher-order nonlinear decomposition for a range of Rossby number (Ro) in idealized nonhydrostatic model simulations, and elucidate wave generation by ageostrophic instabilities of the balanced flow.

The challenges associated with the precise diagnosis of the balanced state, and hence the detection of gravity wave[1] signals, results from the nonlinearity coupling the wave and balanced (or vortical or geostrophic) mode of the linear system. While the former mode is fast and satisfies the gravity wave dispersion relation, the latter evolves only slowly (or even not at all). The numerical methods implemented for the decomposition of balanced and unbalanced flow range from linear to nonlinear methods. Diagnosing only the linear modes does not take into account the nonlinearity of the interactions between balanced and unbalanced motions, which hampers a precise diagnosis of the flow field. Nonlinear decomposition methods, on the other hand, include the nonlinear interactions between the balanced and unbalanced motions, and can thus provide a consistent diagnosis of the two motions. However, the practical implementation of the nonlinear methods can at times be numerically challenging. Such methods are often based on modal expansion, e.g., Machenhauer (1977), Baer and Tribbia (1977), and Warn et al. (1995), but there are exceptions, e.g., Viúdez and Dritschel (2004) and Masur and Oliver (2020). Although the mathematical existence of an exact decomposition is under dispute, the practical implication of the nonexistence of a balanced mode might be minor. For simple surrogate models

Corresponding author: Manita Chouksey, manita.chouksey@uni-hamburg.de

[1] The term "internal gravity wave" or "gravity wave" in this article also includes inertia–gravity waves.

DOI: 10.1175/JPO-D-21-0115.1

it can be in fact shown that an exact decomposition into slow (balanced) and fast (wave) manifolds is not possible (Vanneste 2013), although such a proof for the more complex and relevant system is still missing.

Nonlinear methods such as nonlinear normal mode initialization techniques, e.g., by Machenhauer (1977), implemented in Chouksey et al. (2018), and by Baer and Tribbia (1977), implemented in Kafiabad and Bartello (2016, 2018), include the nonlinearity of the flow field. However, the diagnosed unbalanced part based on these nonlinear methods is accurate only to first order in Ro. This residual signal, interpreted as the unbalanced part, can in fact still be related to the so-called slaved modes as shown by higher-order nonlinear decomposition by Eden et al. (2019a) based on the higher-order expansion in Ro as in Warn et al. (1995). The slaved mode is part of the balanced flow—so it is slowly evolving—but consists of linear wave modes, and is related to the nonlinear coupling between both modes (Vanneste 2013). It is highly possible that gravity waves apparently found in previous model (e.g., Plougonven and Snyder 2007) and laboratory (e.g., Williams et al. 2008) experiments are in fact related to such slaved modes. Nonlinear decomposition methods going beyond first order are therefore important to diagnose and interpret gravity wave generation from balanced flow, even though the balanced mode might not exist in a strict mathematical sense.

In Eden et al. (2019a), gravity wave emission from the balanced flow is diagnosed up to fourth order in Ro using nonlinear modal decomposition, implemented in a single layer model and a primitive equation model. In both the cases the true wave-related signal only appears at higher orders in Ro from the decomposition method, thus showing very weak wave emission (or none at all). The wave signal only gets more prominent for cases with higher Ro. At the first order in Ro, which is equivalent to quasigeostrophic balanced state and the balanced mode obtained by Machenhauer (1977), the diagnosed apparently unbalanced motion comprises of the so-called slaved modes, and the actual "real" wave signal is in fact negligible for small values of Ro in Eden et al. (2019a). The residual wave signal seen at larger Ro is shown to be related to convective or symmetric instability, rather than spontaneous loss of balance.

Here, we revisit the generation of gravity waves in a balanced sheared flow as in Eden et al. (2019a) and focus on the role of convective and symmetric instability for wave generation. To allow for a more realistic simulation of those instabilities, we use a nonhydrostatic model instead of a primitive equation model as in Eden et al. (2019a). In this respect, we also need to report that an error occurred in Eden et al. (2019a): the scaled condition for static instability is not $\partial_z b < -1$ but $\partial_z b < -1/\mathrm{Ro}$, where b denotes scaled buoyancy. That means that in the simulations of Eden et al. (2019a) showing gravity wave emission, static instability was in fact absent, but symmetric instability was important. Therefore, we investigate such cases with gravity wave emission in more detail here. To explain the gravity wave emission we detect in the model experiments, we compare with nonhydrostatic stability analysis featuring ageostrophic unstable modes which obtain finite growth rates at large Ro.

Section 2 describes the stability analysis applied on the classical Eady case with vertical shear and on a jet-like case with both vertical and lateral shear. This is followed by section 3, where the modes obtained from linear stability analysis are balanced up to second order in Ro using nonlinear decomposition, and the resulting balanced state is used to initialize the experiments with jet-like mean flow. In another set of experiments, the jet-like mean flow is also initialized with ageostrophic unstable modes. The diagnosed unbalanced residual is used to quantify wave energy and obtain energy spectra. The results are followed by section 4 that concludes the article with a discussion and summary.

2. Stability analysis

We discuss in this section some results from a stability analysis of the mean flow used in the simulations of shear instability in Eden et al. (2019a). We begin the discussion with the classical vertical shear instability case considered, e.g., by Eady (1949), Stone (1966), and Molemaker et al. (2005), and include later lateral shear as in Eden et al. (2019a). The starting point of the discussion is the momentum equation in Boussinesq approximation which is given by

$$\partial_t \mathbf{u} + f\,\underline{\mathbf{u}} + \nabla p = -(\mathbf{u}\cdot\nabla\mathbf{u} + w\partial_z\mathbf{u}),\ \partial_t w + \partial_z p - b = -(\mathbf{u}\cdot\nabla w + w\partial_z w). \tag{1}$$

Note that a factor ρ_0 is absorbed in the pressure p, that all vectors here are two-dimensional (except eigenvectors below), and that the hook operator in $\underline{\mathbf{u}}$ denotes anticlockwise rotation of $\mathbf{u}$ by 90°. Mass conservation reduces to $\nabla\cdot\mathbf{u} + \partial_z w = 0$ and simplification of the thermodynamics of the fluid under consideration leads to a conservation equation for buoyancy b given by

$$\partial_t b + w\tilde{N}^2 = -(\mathbf{u}\cdot\nabla b + w\partial_z b). \tag{2}$$

The constant stability frequency $\tilde{N}$ results from the stratification of a mean flow. Friction and mixing are ignored here for simplicity.

Introducing L, H as vertical and horizontal scales, $T = 1/\Omega$ as time scale, where Ω is the magnitude of the Coriolis parameter f, and U as horizontal velocity scale, using the hydrostatic and geostrophic balance for the scaling of buoyancy and pressure, the continuity equation for the scaling of w, and dropping primes, we obtain the scaled Boussinesq equations as

$$\partial_t \mathbf{u} + f\,\underline{\mathbf{u}} + \nabla p = -\mathrm{Ro}(\mathbf{u}\cdot\nabla\mathbf{u} + w\partial_z\mathbf{u}), \tag{3}$$

$$\partial_t w + (\partial_z p - b)/\delta^2 = -\mathrm{Ro}(\mathbf{u}\cdot\nabla w + w\partial_z w), \tag{4}$$

$$\partial_t b + N^2 w = -\mathrm{Ro}(\mathbf{u}\cdot\nabla b + w\partial_z b), \tag{5}$$

supplemented by the diagnostic relation $\nabla\cdot\mathbf{u} + \partial_z w = 0$, with the Rossby number $\mathrm{Ro} = U/(L\Omega)$ and $N = \mathrm{Ro}/\mathrm{Fr} = L_r/L$, where Fr denotes the Froude number $\mathrm{Fr} = U/(\tilde{N}H)$ and $L_r = \tilde{N}H/\Omega$ the Rossby radius. $f = 1$ was kept for reference, and we also set $N = 1$ throughout the following. The aspect ratio $\delta = H/L$ is assumed to be small but independent of Ro. The scaled background stratification $\bar{b}(z)$ is given by $N^2 z/\mathrm{Ro}$. The linear system of Eqs. (3)–(5) supports gravity

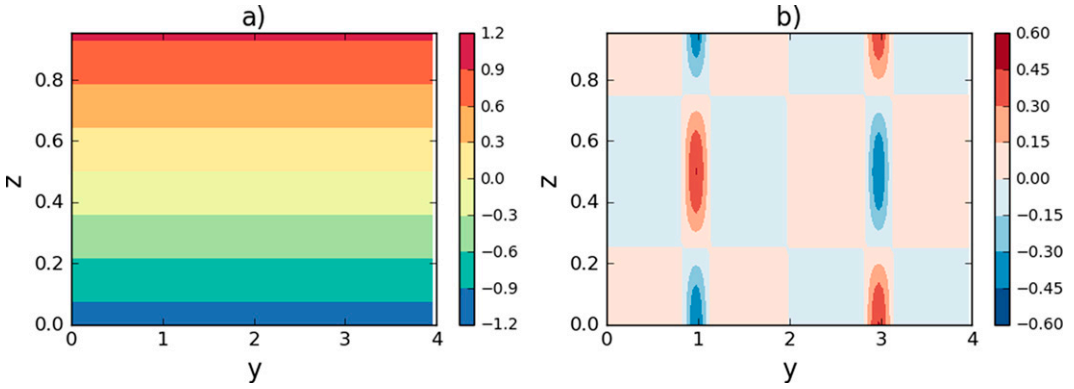

FIG. 1. (a) Zonal velocity of the Eady-like mean flow. (b) Zonal velocity of the jet-like mean flow.

waves with frequencies $1 \le |\omega| \le 1/\delta$ and the geostrophic mode with $\omega = 0$.

a. *Eady-like mean flow*

For a stability analysis as, e.g., in Eady (1949) and Stone (1966), it is common to define a vertically sheared mean flow such as $\mathbf{u}_b = (U_0 z - U_0/2, 0, 0)^T$ with constant U_0 and $0 \le z \le 1$, and buoyancy and pressure in thermal wind and hydrostatic balance with $\mathbf{u}_b$. Such a mean flow is shown in Fig. 1a. Adding a perturbation to the Eady-like mean flow, followed by linearization, then applying the ansatz $\mathbf{u} = \hat{\mathbf{u}}(z)\exp i(k_x x + k_y y - \omega t)$, etc. to the perturbed variables, and solving for the most unstable mode with largest $\mathrm{Im}(\omega)$leads to the classical vertical shear instability solution. Using the scaled Boussinesq equations Eqs. (3)–(5), the growing modes for small Ro are very similar to the classical solution by Eady (1949) based on the quasigeostrophic equations (obtained for $\mathrm{Ro} \ll 1$ and $\delta \ll 1$, but fixed relation $\mathrm{Ro} \sim \mathrm{Fr}$, $L_r \sim L$, see below),

$$\omega/k_x = \mathrm{Ro} U_0 \sqrt{\frac{1}{4} + d^2 - d \coth 1/d} \tag{6}$$

with $d = |f|/(N\sqrt{k_x^2 + k_y^2})$ and with a maximal growth rate (scaled by Ro) $\mathrm{Im}(\omega)/\mathrm{Ro} \approx 0.3 U_0$ at a zonal wavenumber $k_x \approx 1.6$ (for $f = N = 1$). Accordingly, this mode is balanced and slow with frequencies $\mathrm{Re}(\omega) \approx 0$, and is often called the geostrophic unstable mode. This unstable mode corresponds to the classical baroclinic instability. Figures 2a and 2b shows the growth rate $\mathrm{Im}(\omega)$ for small Ro evaluated numerically for the Boussinesq equations for the mean state shown in Fig. 1a. For small Ro it is almost identical to the quasigeostrophic version with vanishing, thus slow (intrinsic) frequency $\mathrm{Re}(\omega)$.

For larger Ro, the maximum $\mathrm{Im}(\omega)$ and corresponding k_x get slightly smaller in the Boussinesq equations compared to Eq. (6), but more importantly, another unstable mode appears: Figs. 2c and 2d shows the growth rate (scaled by Ro) $\mathrm{Im}(\omega)/\mathrm{Ro}$ for $\mathrm{Ro} = 0.5$ and $U_0 = 2$. For this value of U_0 and Ro, the potential vorticity of the mean flow $Q = f[1 - \mathrm{Ro}^2(\partial_z u)^2/N^2]$ just vanishes (while $Q > 0$ for smaller U_0 or Ro), i.e., the condition for symmetric instability is satisfied. Besides the large growth rates $\mathrm{Im}(\omega)/\mathrm{Ro}$ of the geostrophic unstable mode with frequencies $\mathrm{Re}(\omega) \approx 0$, another growing mode appears for large zonal wavenumbers k_x which is fast, i.e., with the possibility of large positive and negative frequencies $\mathrm{Re}(\omega)$ as seen in Fig. 2d. Note that for a balanced mode, a frequency $|\mathrm{Re}(\omega)| > \mathrm{Ro}$ would be inconsistent with the time scale separation between fast and slow modes, which we assume in the balanced flow definition of Warn et al. (1995). This fast unstable mode in the Eady-like mean flow for large Ro is not present in the quasigeostrophic case Eq. (6), and was accordingly called the ageostrophic unstable mode by Molemaker et al. (2005). The maximal growth rate $\mathrm{Im}(\omega)/\mathrm{Ro}$ of the ageostrophic unstable mode is also shown as a function of Q and Ro in Fig. 2e and Fig. 2f, respectively. Note that the growth rates of this mode are much smaller for $Q > 0$, i.e., for smaller Ro or U_0 but stay finite (Fig. 2e). We hypothesize that the ageostrophic unstable mode is related to the gravity wave emission in the model simulations of Eden et al. (2019a).

b. *Jet-like mean flow*

We aim to make now the Eady-like mean flow a little more general (more complex) by using a jet-like mean flow, where we add also lateral shear to the vertical shear in the mean flow. The jet-like mean flow is shown in Fig. 1b and is given by $\mathbf{u}_b(y,z) = \{\exp[-(y-1.25)^2/L_{\mathrm{jet}}^2 - (y-3.75)^2/L_{\mathrm{jet}}^2], 0\}^T \cos(2\pi z)$ with $L_{\mathrm{jet}} = 0.16$ if not otherwise noted, and $0 \le z \le 1$, $0 \le y \le 4$. This mean state is similar to the one used in Eden et al. (2019a), but with different (larger) amplitude. The added lateral shear, in addition to the vertical shear, might be seen as a representation of geostrophic flow after frontogenesis, allowing us to investigate the wave generation from instabilities in the full three dimensions of the flow. Instead of rigid lids at the top and bottom as in the Eady-like situation, we use here triple periodic boundary conditions. Due to the lateral shear, the meridional gradient of potential vorticity of the mean flow $\partial_y Q$ has several zero crossings in the jet-like mean flow, such that the necessary condition for instability is satisfied (while in the Eady-like case $\partial_y Q = 0$ and the necessary condition is satisfied by the vertical boundary conditions). Because of the lateral shear, we also use the ansatz

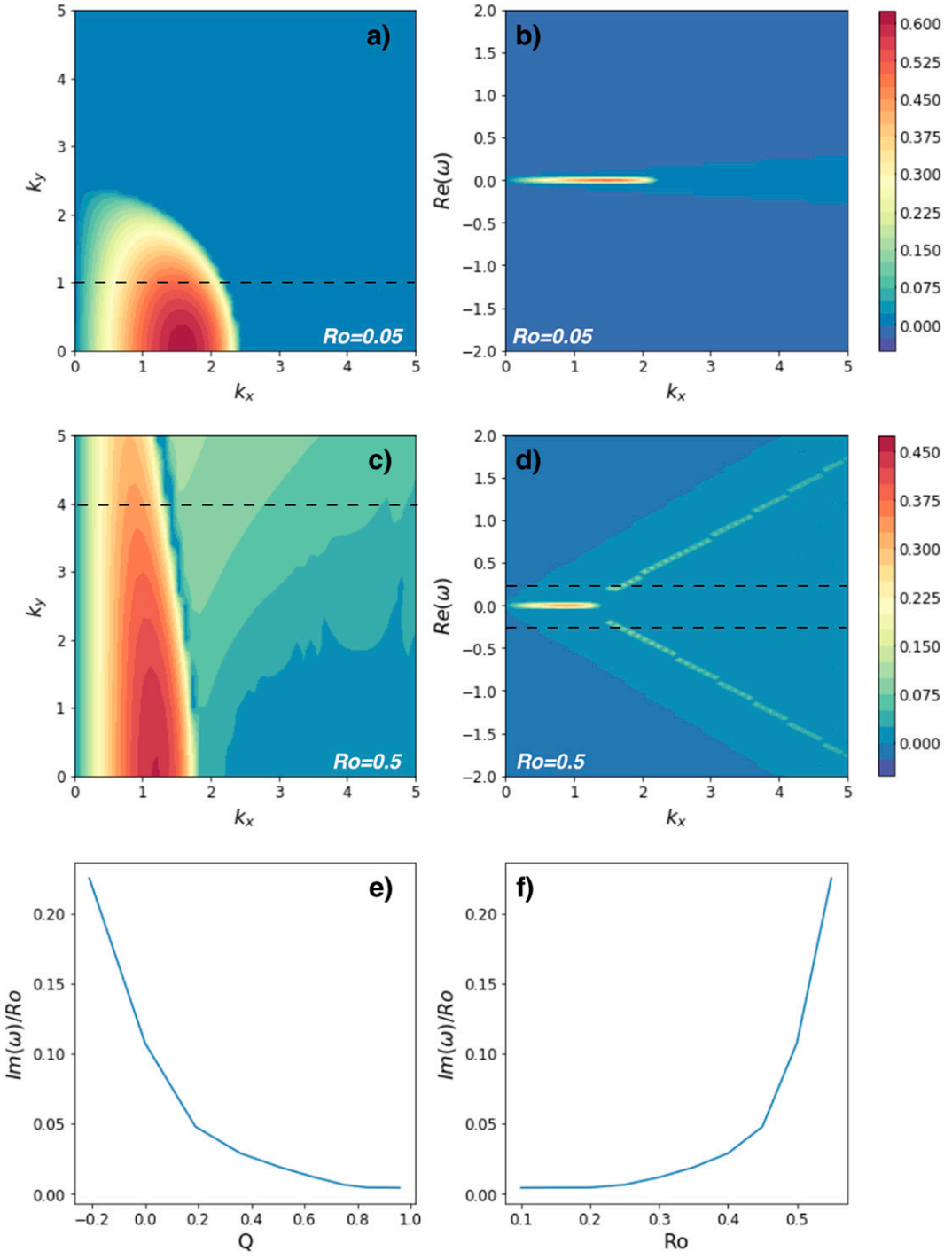

FIG. 2. (a) Largest growth rate Im(ω)/Ro as function of k_x and k_y for the Eady-like mean flow and Ro = 0.05. (b) Im(ω)/Ro for $k_y = 1$ as function of k_x and frequency Re(ω). (c) Largest growth rate Im(ω)/Ro as function of k_x and k_y for the Eady-like mean flow and Ro = 0.5. (d) Im(ω)/Ro for $k_y = 4$ as function of k_x and frequency Re(ω). Black dashed lines in (a) and (c) indicate the slices at k_y taken for (b) and (d). (e),(f) Maximal Im(ω)/Ro with $|\text{Re}(\omega)| > 0.2$ [marked by black dashed lines in (d)] as a function of Q and Ro.

$\mathbf{u} = \hat{\mathbf{u}}(y,z)\exp i(kx - \omega t)$, etc. for the perturbations. The method to obtain ω and $\hat{u}(y,z)$ is detailed in the appendix.

Figure 3 shows that the largest growth rates are still $\mathrm{Im}(\omega)/\mathrm{Ro} \approx 0.5$ and occur for frequencies $\mathrm{Re}(\omega) \approx 0$, but now for larger zonal wavenumber with a maximal growth rate at $k \approx 5$. The larger k compared to the Eady case is mostly due to the different vertical shear. However, it appears that there are also plenty of other modes present with finite growth rates $\mathrm{Im}(\omega)/\mathrm{Ro}$ and also with frequencies $|\mathrm{Re}(\omega)| > \mathrm{Ro}$ for $\mathrm{Ro} \geq 0.2$ (Figs. 3g,h). As stated earlier, a frequency $|\mathrm{Re}(\omega)| > \mathrm{Ro}$ for the balanced mode would be inconsistent with the definition of the balanced flow that we assume here. Going from $\mathrm{Ro} = 0.2$ to $\mathrm{Ro} = 0.3$ the condition for symmetric instability in the mean flow is given, i.e., $Q < 0$. The fast unstable modes with $|\mathrm{Re}(\omega)| > \mathrm{Ro}$ for $\mathrm{Ro} \geq 0.2$ appear to correspond to the ageostrophic unstable modes in the Eady-like case.

For the limit of $\mathrm{Ro} \ll 1$ and $\delta \ll 1$ (but fixed relation $\mathrm{Ro} \sim \mathrm{Fr}$, $L_r \sim L$), the quasigeostrophic approximation is valid and yields from Eq. (3) to Eq. (5) a single governing equation $\partial_t q_{\mathrm{qg}} = -\mathrm{Ro}\,\underline{\nabla}\psi \cdot \nabla q_{\mathrm{qg}}$ with quasigeostrophic potential vorticity $q_{\mathrm{qg}} = \nabla^2\psi + (f^2/\mathrm{N}^2\partial_{zz}\psi)$ and the quasigeostrophic streamfunction ψ with $\underline{\nabla}\psi = \mathbf{u}$ and $f\partial_z\psi = b$. Using the jet-like mean flow, linearization and solving numerically for the fastest growing modes (also shown in Fig. 3) yields similar growth rates and frequencies as for the nonhydrostatic case with small Ro. The finite (extrinsic) $\mathrm{Re}(\omega)$ are only due to a Doppler shift by the mean flow and do not indicate the emergence of a fast mode which is excluded in the quasigeostrophic approximation. Going to larger Ro in the nonhydrostatic case, however, the growth rates differ. We therefore interpret the unstable modes for large Ro, not seen in the quasigeostrophic case, as the equivalent of the ageostrophic unstable modes in the Eady-like case.

3. Nonlinear model experiments

We now use the mean flow and the geostrophic unstable mode with small amplitude as initial condition in a fully nonlinear model and use the flow decomposition by Warn et al. (1995) to detect gravity wave generation, as implemented in Eden et al. (2019a). The numerical model solves the Boussinesq system Eqs. (3)–(5) on a triple periodic domain with extent of $4 \times 4 \times 1$. We use $1000 \times 1000 \times 120$ grid points and small biharmonic friction and mixing in the horizontal and vertical direction with horizontal and vertical parameters of $\mathrm{Ro}\Delta x^3$ and $\mathrm{Ro}\Delta z^3$, respectively, and a spectral solver for the pressure. We use different values of Ro, no forcing, and as initial conditions the jet-like mean state shown in Fig. 1b, where a small perturbation is superimposed, which is taken from the eigenvector with corresponding eigenvalue shown in Fig. 3 as small circles at $\mathrm{Ro}(\omega)/\mathrm{Ro} = 0$, i.e., the geostrophic unstable mode. The eigenvector with largest growth rate $\mathrm{Im}(\omega)$ close to the middle of the white circle at $k = 5$ is chosen. The eigenvector from the stability problem is interpolated on the finer grid of the numerical model, and afterward balanced up to second order in Ro using the method by Warn et al. (1995) that is also used in Eden et al. (2019a). This is done to guarantee that no gravity waves are excited by the initial conditions, but only (eventually) due to the growing geostrophic unstable mode. There is, however, only a small adjustment to the perturbation by the balancing method necessary. We may call this perturbation the near optimal geostrophic unstable mode for the numerical simulations.

a. Initialization with the geostrophic unstable mode

The geostrophic unstable mode quickly grows in all simulations as predicted by the stability analysis. Figure 4 shows the distribution of scaled potential vorticity

$$Q = f + \frac{f\mathrm{Ro}}{N^2}\partial_z b + \mathrm{Ro}(\partial_x v - \partial_y u) + \frac{\mathrm{Ro}^2}{N^2}\left[(\partial_x v - \partial_y u)\partial_z b - (\partial_z v)\partial_x b + (\partial_z u)\partial_y b\right] + \frac{\mathrm{Ro}^2\delta^2}{N^2}\left[(\partial_y w)\partial_x b - (\partial_x w)\partial_y b\right] \quad (7)$$

at all grid points in three simulations with different Ro after the onset of the baroclinic instability at $t = 6/\mathrm{Ro}$. While for $\mathrm{Ro} = 0.1$, all values of Q stay larger than 0.5, for $\mathrm{Ro} = 0.2$ the smallest values of Q become small, and for $\mathrm{Ro} = 0.3$ even negative values of Q occur, indicating symmetric instabilities of the flow. Note that the condition for static instability $\partial_z b < -1/\mathrm{Ro}$ is never satisfied in the simulations.

Figure 5 shows the vertical velocity w at mid depth in the domain after the onset of the baroclinic instability at $t = 6/\mathrm{Ro}$ for different Ro. The geostrophic unstable mode leads to a meandering of the mean flow, which is clearly seen also in w. The vertical velocity w is small and of the order of Ro in all three simulations in accordance with quasigeostrophic scaling. The lower row of Fig. 5 shows the first-order vertical velocity w_1 of the balanced mode estimated using the method by Warn et al. (1995) as in Eden et al. (2019a), which is almost identical to the actual w for all three Ro. Note that w_1 corresponds to the first-order vertical velocity in the quasigeostrophic approximation.

Figure 6 shows the difference between the actual w and w_1 for all three simulations, which is as expected on the order of Ro^2 in all cases. For $\mathrm{Ro} = 0.1$, the second-order vertical velocity w_2 of the balanced mode is still almost identical to $w - w_1$, such that it still corresponds entirely to the balanced mode, i.e., no gravity waves can be detected up to Ro^2. The same remains true for the third order (not shown). For $\mathrm{Ro} = 0.2$, however, a small difference between $w - w_1$ and w_2 begins to show up, which is even more pronounced in the simulations with $\mathrm{Ro} = 0.3$. This means that even though we have initialized the model with a balanced flow and the geostrophic unstable mode, gravity waves are generated during the instability at large Ro. We relate this small gravity wave generation at Ro^2 to the symmetric instability and the ageostrophic unstable mode, which is not present in the initial conditions but excited by the fully developed instability.

To quantify the energy associated with the wave generation in the experiments initialized with the geostrophic unstable mode (Figs. 5 and 6), the residual kinetic energy is shown for

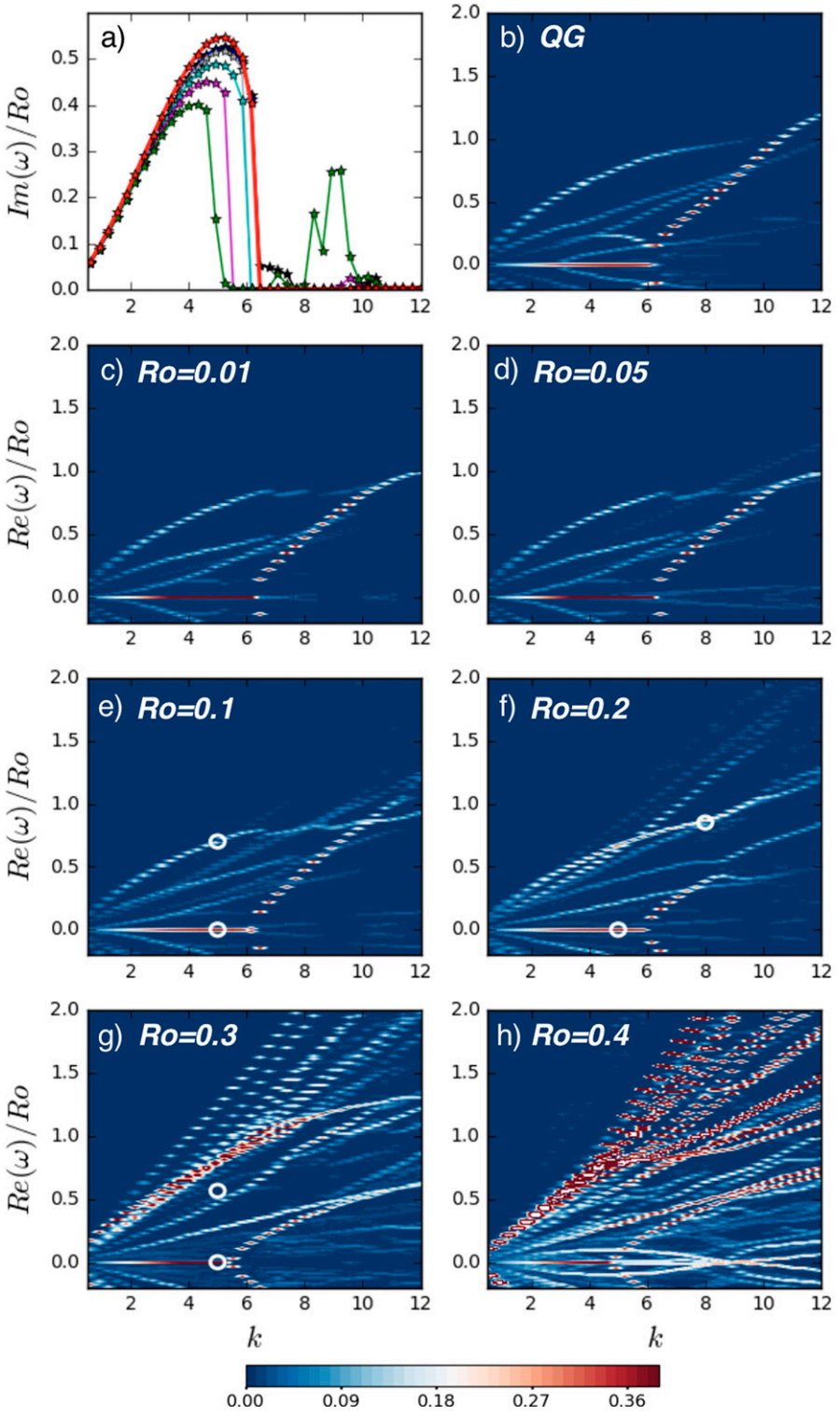

FIG. 3. (a) Largest growth rate Im(ω)/Ro for frequency Re(ω) ≈ 0 as a function of zonal wavenumber k (x axis) and Ro= 0.01 (black), 0.05 (blue), 0.1 (gray), 0.2 (cyan), 0.3 (magenta), 0.4 (green) for the jet-like mean flow. The largest Im(ω)/Ro corresponds to the smallest Ro. Im(ω)/Ro for the quasigeostrophic case is shown by the red line. (b) Im(ω)/Ro for the quasigeostrophic (QG) case. Im(ω)/Ro does not depend on Ro in the quasigeostrophic case. (c)–(h) Largest growth rate Im(ω)/Ro as function of zonal wavenumber k (x axis) and frequency Re(ω)/Ro (y axis) for different Ro.

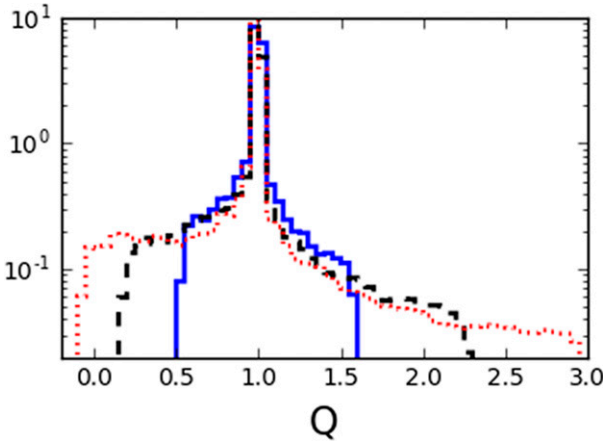

FIG. 4. Normalized distribution of scaled potential vorticity Q at $t = 6/\mathrm{Ro}$ in the jet-like simulations with different Ro (solid blue: Ro = 0.1, dashed black: Ro = 0.2, dotted red: Ro = 0.3).

different Ro and for different orders in Fig. 7. The figure shows the volume integral of the scaled residual kinetic energy, computed as $[(\mathbf{u} - \sum_{i=0}^{n} \mathbf{u}_i)^2 + \delta^2(w - \sum_{i=0}^{n} w_i)^2]/(2\mathrm{Ro}^{2n})$ for $n = 0, 1, 2$, i.e., for the first, second, and third order, where $\mathbf{u}_i$ and w_i are the balanced components at order i. Clearly, the residual energy related to the waves appears more strongly for higher Ro and is enhanced at higher orders. The dependency of the wave emission on Ro appears to be exponential for this configuration, for Ro > 0.15, the function 0.9exp[(Ro − 0.15)/0.08] fits well the highest-order residual in the figure.

b. *Initialization with the ageostrophic unstable mode*

Figure 8 shows simulations at different Ro initialized with modes different from the geostrophic unstable mode used before, indicated by the small circles in Fig. 3 with $\mathrm{Re}(\omega)/\mathrm{Ro} \neq 0$. The model state using such eigenvectors is still balanced up to second order in Ro using the method by Warn et al. (1995), but the intention of these experiments is to come closer to the unstable ageostrophic modes with the initial conditions, while still eliminating all gravity waves at $t = 0$. While for Ro = 0.1 we still see no gravity waves at first order in Ro, in the case of Ro = 0.2 and in particular for Ro = 0.3 we begin to see gravity waves at lowest order.

The wavenumber spectra of the residual energy are shown in Fig. 9 for the experiment with Ro = 0.3, where Fig. 8 indicates strong gravity wave activity. The wavenumber spectra of the residual horizontal kinetic energy $(\mathbf{u} - \sum_{i=1}^{n} \mathbf{u}_i)^2/2$, residual potential energy $(b - \sum_{i=0}^{n} b_i)^2/2N$, and residual vertical kinetic energy $\delta^2(w - \sum_{i=0}^{n} b_i)^2/2$ at $z = 0.3$ and for $n = 0, 1, 2$ as a function of horizontal wavenumber $k = \sqrt{k_x^2 + k_y^2}$ are shown for different orders (first, second, and third). All curves are scaled with the integral of kinetic energy at $n = 0$ and shown in variance preserving form. The peaks in the residual vertical kinetic energy and potential energy spectra at higher wavenumbers affirm the prominent wave activity in this regime seen in Fig. 8.

Further, Fig. 9d shows wave frequency ω estimated from the ratio of vertical to horizontal kinetic energy $R = w^2/(u^2 + v^2)$ [cf. Olbers et al. (2012), section 7.2], i.e.,

$$R = \frac{w^2}{u^2 + v^2} = \frac{\omega^2}{\omega^2 + f^2} \frac{\omega^2 - f^2}{N^2 - \delta^2\omega^2}. \tag{8}$$

The generated waves appear to be near inertial at small k, but at larger wavenumbers the waves appear with larger frequencies reaching up to midfrequencies (maximal frequency is N/δ). The energy across different wavenumbers indicate that the full spectrum of the waves is excited during the process in the experiments shown in Fig. 8. This makes it difficult to relate the genesis mechanism and the excited waves for a given wavenumber. This further suggests that the initial ageostrophic imbalance at $k = 6$ in these experiments may not be directly related to the waves excited across all wavenumbers, and requires further investigation.

It is thus possible to excite gravity waves by an instability of the balanced mode to lowest order, if the condition of symmetric instability is close to be satisfied and ageostrophic unstable modes obtain finite growth rates. This is the main conclusion of this study.

4. Summary and discussion

In this study, we have diagnosed gravity wave emission of vertical and horizontal shear instability in idealized nonhydrostatic model simulations using the nonlinear decomposition method up to third order in Rossby number (Ro) based on Warn et al. (1995) and as implemented in Eden et al. (2019a). In case of geostrophic instability of a well-balanced initial state similar to the classical Eady model, i.e., classical baroclinic instability, the wave emission is negligible up to third order over a range of values for Ro. Only when the model is initialized with a mean flow closer to the so-called ageostrophic instability mode with larger (i.e., faster) frequencies—but still well balanced up to third order in Ro—we do see significant gravity wave emission at the lowest order. This residual wave energy is enhanced at higher orders and for higher Ro, and the dependency of the wave energy emission on Ro appears to be exponential. A wavenumber spectrum of the residual wave energies reveals that a rich spectrum of waves is excited in the flow when initialized with the ageostrophic unstable mode, dominated by inertial to midfrequency waves. The wavenumber of the generated waves and that of the balanced instabilities are thus not related in a straightforward way. The presence of the ageostrophic instability mode with significant growth rates comes along with vanishing (or even negative) potential vorticity of the mean flow, indicative of the possibility of symmetric instability. Thus, we conclude here that gravity waves are only emitted by balanced shear flow to a significant amount in our experiments, if its potential vorticity becomes small or negative, and symmetric and ageostrophic instabilities become possible. This result also points to the weak importance of spontaneous loss of balance for wave generation.

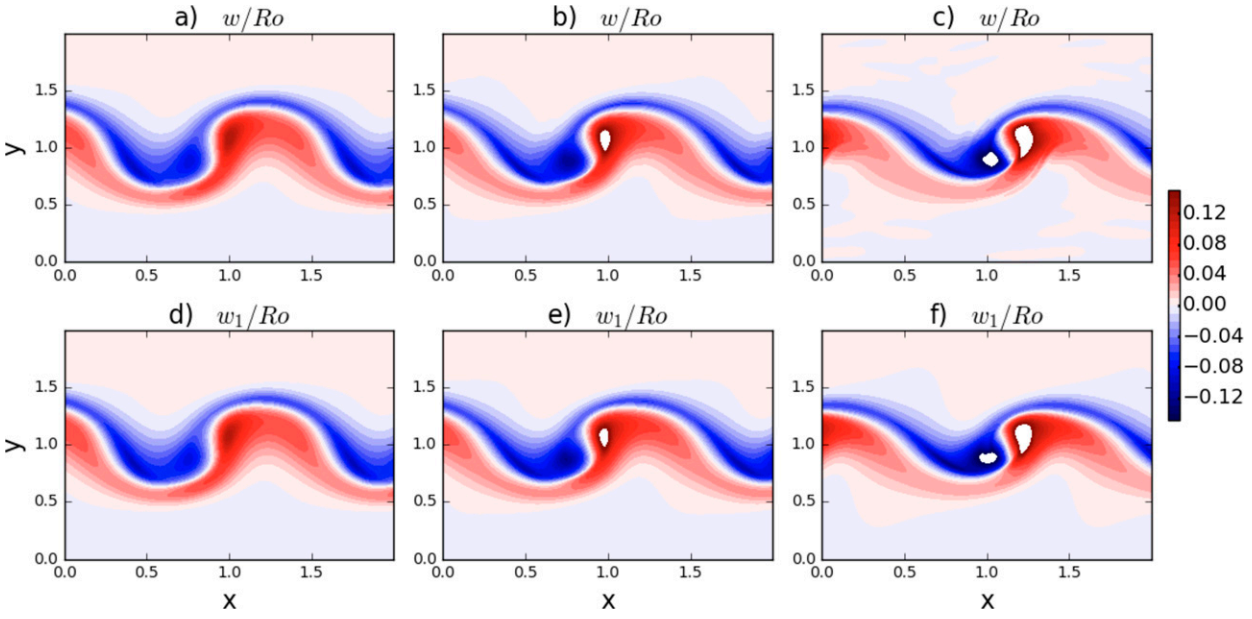

FIG. 5. (top) The w/Ro at $z = 0.3$ and $t = 6$/Ro in the jet-like simulations with different Ro: (a) Ro = 0.1, (b) Ro = 0.2, (c) Ro = 0.3, and initialized with the near optimal geostrophic unstable mode. (d)–(f) As in (a)–(c), but for w_1/Ro.

Besides the role of ageostrophic and shear instabilities, discussed here as well as in Eden et al. (2019a), another mechanism has previously been discussed for spontaneous loss of balance: wave emission in the sense of classical Lighthill radiation (Ford et al. 2000). In a rotating shallow water configuration with small Fr and Ro > 1, Ford et al. (2000) show that Lighthill radiation can indeed occur at high orders, where resonant interactions between waves and the balanced flow can lead to energy transfer. However, the process is only relevant for Ro > 1 and small Fr (Saujani and Shepherd 2002), a dynamical regime which we have not considered here. It can be shown that for Ro < 1, the relevant resonant triad (first order) interactions between waves and balanced flow for the two-dimensional (2D) shallow water equations (as considered by Ford et al. 2000) are exactly vanishing (Eden et al. 2019b). In the ocean and atmospheric flow regimes, values of Ro and Fr are mostly not such that Lighthill radiation can occur, making it a weak candidate mechanism for internal gravity wave generation, although locally Ro may exceed unity while Fr

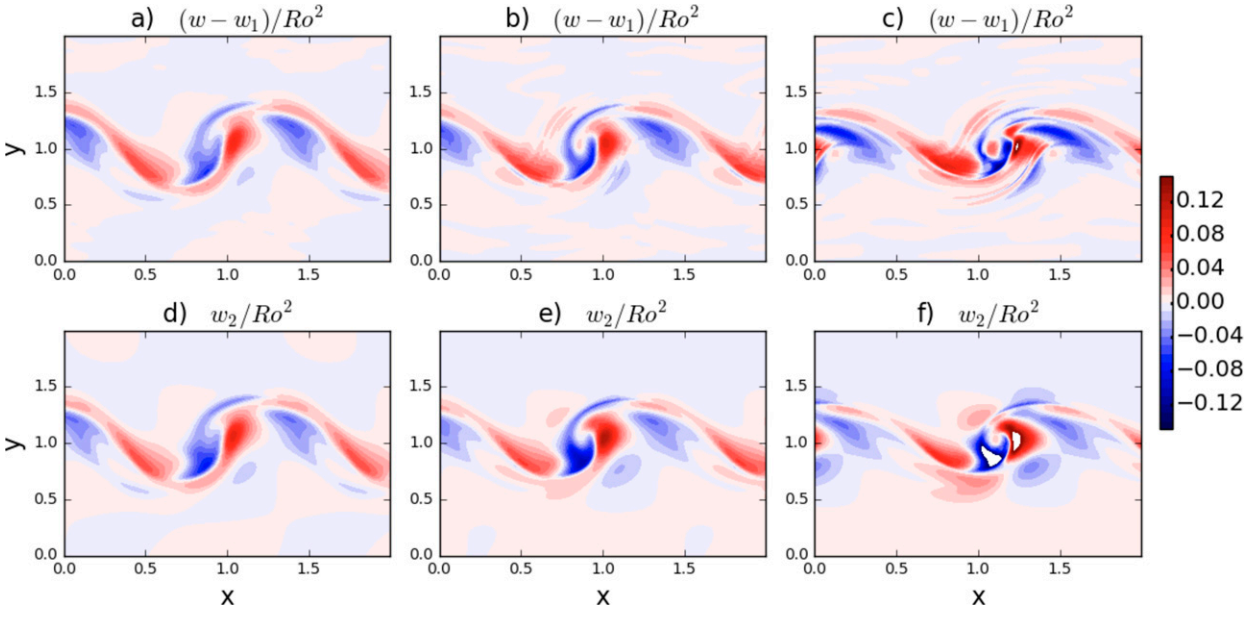

FIG. 6. (top) The $(w - w_1)/\mathrm{Ro}^2$ at $z = 0.3$ and $t = 6$/Ro in the jet-like simulations with different Ro: (a) Ro = 0.1, (b) Ro = 0.2, (c) Ro = 0.3, and initialized with the near optimal geostrophic unstable mode. (d)–(f) As in (a)–(c), but for w_2/Ro^2.

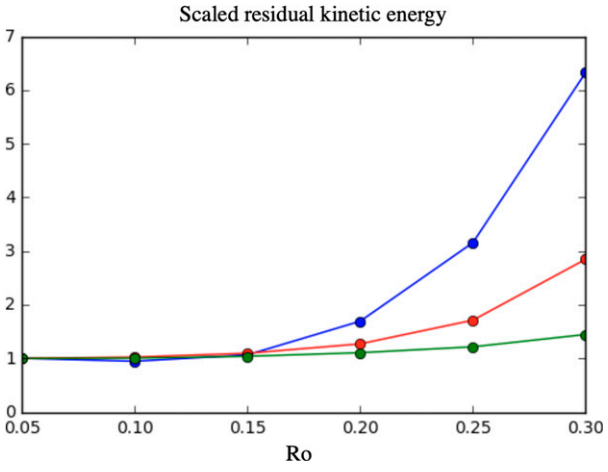

FIG. 7. Volume integral of the scaled residual kinetic energy $[(\mathbf{u} - \sum_{i=0}^{n}\mathbf{u}_i)^2 + \delta^2(w - \sum_{i=0}^{n}w_i)^2]/(2\mathrm{Ro}^{2n})$ for $n = 0, 1, 2$ for the first (green), second (red), and third (blue) order, for the experiments initialized by the geostrophic unstable mode shown in Fig. 5 and Fig. 6. All curves are scaled with their values at Ro = 0.05.

stays small, and Lighthill radiation may become relevant. The importance of Lighthill radiation thus still needs quantification.

Other processes can also lead to energy transfers between waves and balanced flow, such as stimulated wave emission (Gertz and Straub 2009), or interaction with boundaries (Dewar and Hogg 2010; Chouksey 2018). The latter we do not discuss here. In the former, a preexisting wave field interacts with the balanced flow. In such a stimulated emission scenario, Gertz and Straub (2009) find large energy transfers from the 2D to the three-dimensional (3D) circulation at large Ro, where the 3D (2D) flow field is interpreted as unbalanced (balanced) motion. By further exploring the process of stimulated emission, Rocha et al. (2018) substitute the 2D circulation with a quasigeostrophic model, excluding ageostrophic instabilities as discussed here. Instead of a full model, they use a phase-averaged wave equation model interacting with the quasigeostrophic flow and still find significant energy transfers between waves and mean flow. Barkan et al. (2017) also reports notable energy transfer from balanced flow to near-inertial waves by stimulated emission, where the preexisting near-inertial waves are externally forced by winds at the inertial frequency.

Eden et al. (2019b) find only weak energy transfer between waves and balanced flow for Ro < 1 and initially vanishing wave energy in 3D flow in a numerical evaluation of the scattering integral, generated also only by nonresonant triad interactions. Stimulated wave emission related to a preexisting gravity wave field appears thus also difficult to happen by resonant triad interactions because of the large frequency of gravity waves. If so, this may only be possible at large Ro as for Lighthill radiation. The analysis in Eden et al. (2019b), our own preliminary analysis (not shown), and the study by Savva et al. (2021) indicate that there is in fact no resonant triad interaction of waves and balanced flow to first order, but only elastic scattering which redistributes energy within the wave field. A preexisting wave field, driven by external forces, may thus drain energy from the balanced flow only by nonresonant triad interactions, but the rate and sign of the transfer at which this might happen remain unclear.

In any case, we want to stress that careful diagnosis is necessary to evaluate spontaneous or stimulated wave emission in model simulations, laboratory experiments, or even observations.

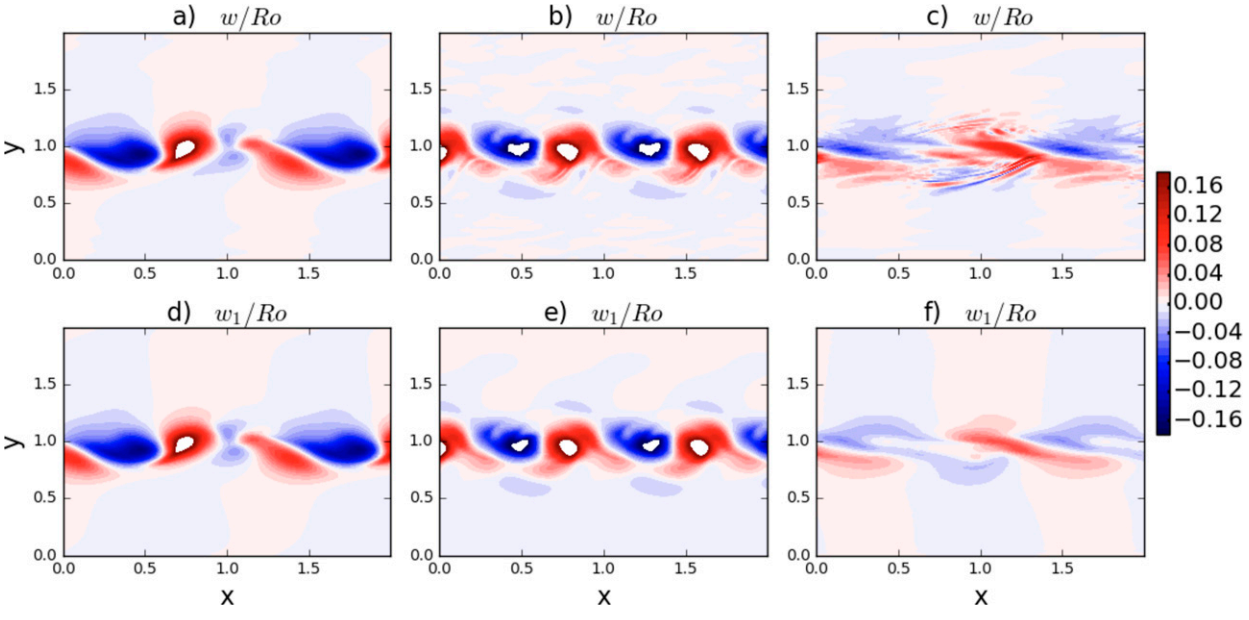

FIG. 8. (top) The w/Ro at $z = 0.3$ and (a) Ro = 0.1 at $t = 10$/Ro, (b) Ro = 0.2 at $t = 10$/Ro, (c) Ro = 0.3 at $t = 7.5$/Ro in the jet-like simulations with different Ro and initialized with the modes with nonzero Re(ω)/Ro as indicated in Fig. 3 and detailed in the text. (d)–(f) As in (a)–(c), but w_1/Ro.

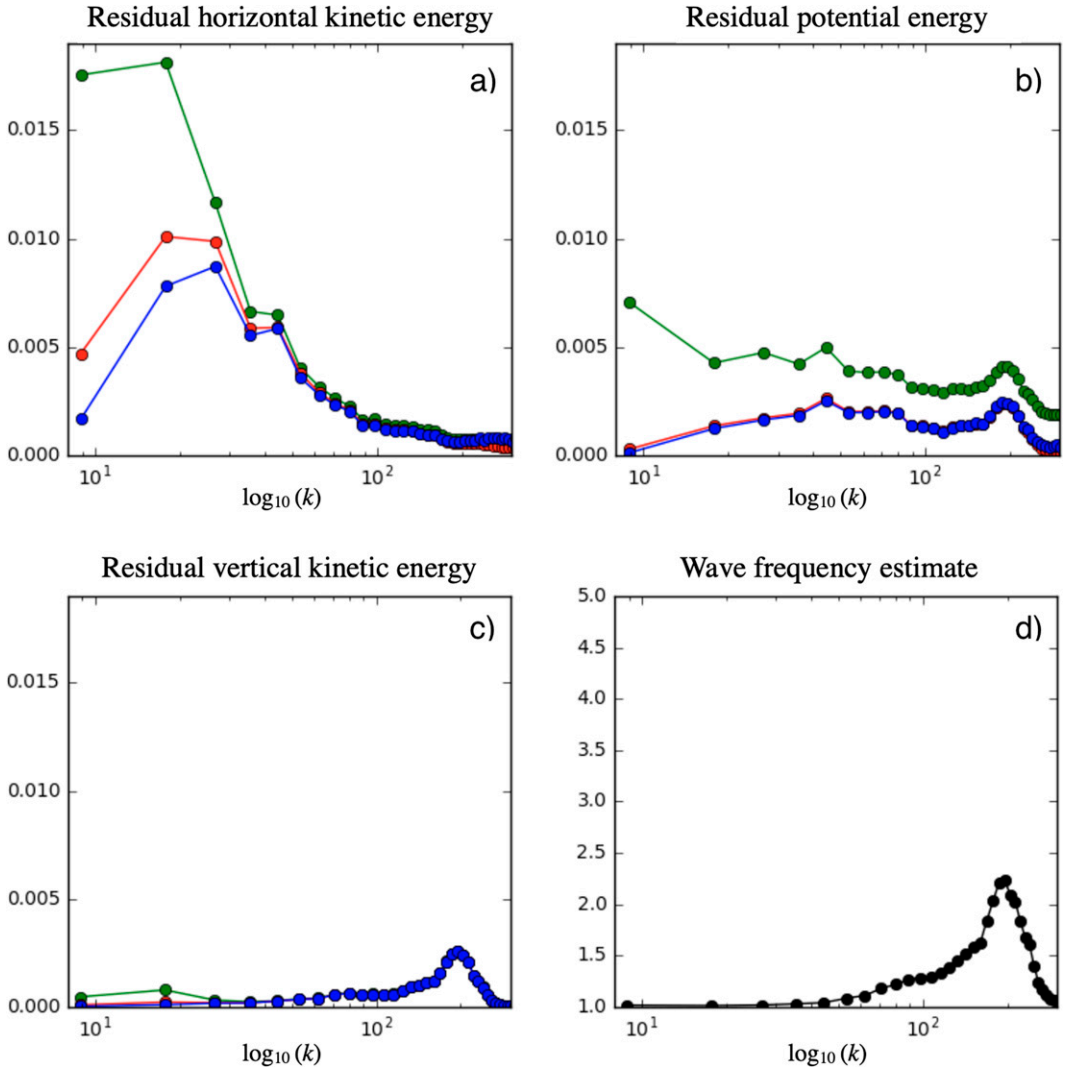

FIG. 9. Wavenumber spectra for the residual velocities for the experiment with Ro = 0.3 shown in Fig. 8c. (a) Residual horizontal kinetic energy $(u - \sum_{i=1}^{n} u_i)^2/2$, (b) potential energy $(b - \sum_{i=0}^{n} b_i)^2/2N$, and (c) vertical kinetic energy $\delta^2(w - \sum_{i=0}^{n} b_i)^2/2$ at $z = 0.3$, shown as function of wavenumber modulus $k = \sqrt{k_x^2 + k_y^2}$ for $n = 0$, 1, 2 for the first (green), second (red), and third (blue) order. Shown is energy E in variance preserving form as kE. All curves are scaled with the integral of kinetic energy at $n = 0$. (d) An estimate of the wave frequency obtained from the ratio $R = w^2/(u^2 + v^2)$.

Often the signal seen in vertical velocity or the divergence field as in, e.g., Plougonven and Snyder (2007) is not related to actual wave motion but to the slaved mode as in our Fig. 5, which is still part of the balanced mode.

This article is a follow up of our previous article Eden et al. (2019a), that investigates the gravity wave emission from an initially balanced sheared flow of similar structure as here but for a primitive equation model. In this study we have extended this analysis of wave emission from a simplified model setup to the more realistic nonhydrostatic model setup, and examine the role of symmetric and ageostrophic instabilities for the wave emission in more detail. In Eden et al. (2019a) we reported that when the flow becomes convectively unstable, we see significant gravity waves emission in the primitive equation model. However, the condition for static instability which we used in Eden et al. (2019a) is not correct and the correct condition was never satisfied in the simulations. The gravity waves seen there are not caused by static instability but in fact by symmetric instability, similar to the case we find here. Therefore, this article reinforces the conclusion from our previous work Eden et al. (2019a): spontaneous wave emission is in general very weak and only symmetric or ageostrophic instability of the mean flow appears to be able to trigger significant wave generation at the lowest order.

Acknowledgments. We thank two anonymous reviewers for their helpful comments. This study is a contribution to

the project W2 and W6 of the Collaborative Research Centre TRR 181 "Energy Transfers in Atmosphere and Ocean" funded by the Deutsche Forschungsgemeinschaft (DFG, German Research Foundation) - Projektnummer 274762653.

APPENDIX

Numerical Stability Analysis

The method to obtain the eigenvalue ω and eigenvectors of the stability analysis follows the one used in Thomsen et al. (2014). We add to the system Eqs. (3)–(5) the scaled pressure equation

$$\partial_t p = -c^2(\nabla \cdot \mathbf{u} + \partial_z w) \tag{A1}$$

with the scaled sound speed $c = \mathrm{Ro}/\mathrm{Ma}$ and the Mach number $\mathrm{Ma} = U/c_s \ll \mathrm{Ro}$, where $c_s = (\partial\rho/\partial p)^{-1/2}$ is the actual sound speed related to the compressibility of seawater. This prognostic pressure equation replaces the diagnostic continuity equation. We use an artificially reduced value of $c = 50$ and found no sensitivity of the results on this choice.

Defining a mean flow as stated above for the Eady-like case with $\mathbf{u}_b = [U(z), 0, 0]^{\mathrm{T}}$ in thermal wind balance, linearization, and using the ansatz $\exp i(kx + ly - \omega t)$ for the perturbation variables yields the system

$$\mathbf{Ma} = \omega\mathbf{a},\ \mathbf{M}(z) = \begin{pmatrix} k\mathrm{Ro}U & if & -i\mathrm{Ro}\partial_z U & 0 & k \\ -if & k\mathrm{Ro}U & 0 & 0 & l \\ 0 & 0 & k\mathrm{Ro}U & i/\delta^2 & -i\partial_z/\delta^2 \\ 0 & i\mathrm{Ro}f\partial_z U & -iN^2 & k\mathrm{Ro}U & 0 \\ c^2k & c^2l & -ic^2\partial_z & 0 & 0 \end{pmatrix} \tag{A2}$$

for the vector $\mathbf{a}(z) = (u, v, w, b, p)^{\mathrm{T}}$. Discretization in z with $N = 100$ points from $z_{n=1}$ to $z_{n=N}$, yields a sparse algebraic eigenvalue problem, which can be solved for given wavenumber vector (k, l). Variables p_n, u_n, v_n and b_n are at positions z_n, while the vertical velocity w_n is between p_n and p_{n+1}. Grid spacing is constant and given by $\Delta_z = z_{n+1} - z_n$. We use horizontally double periodic boundary conditions and rigid lids at top and flat bottom for the Eady-like case. The rank of the resulting square matrix for which eigenvalues and eigenvectors need to be found is $5N$. Eigenvalues related to sound (and Lamb) waves in the system are easily identified due to their large frequency and sorted out.

The procedure for the jet-like case follows closely the Eady-like case; the difference being that the ansatz $\exp i(kx - \omega t)$ for the perturbations leads to $\mathbf{M} = \mathbf{M}(y, z)$, and that we use triple periodic boundary conditions. Discretization in z with $N_z = 24$ points from $z_{n=1}$ to $z_{n=N_z}$ and in y with $N_y = 100$ points from $y_{j=1}$ to $y_{j=N_y}$, yields an algebraic eigenvalue problem, which can be solved for given wavenumber k. Discrete variables $p_{j,n}$, $u_{j,n}$ and $b_{j,n}$ are at the discrete positions z_n and y_j. Vertical velocity $w_{j,n}$ is at vertical position between $p_{j,n}$ and $p_{j,n+1}$, while $v_{j,n}$ is at meridional position between $p_{j,n}$ and $p_{j+1,n}$. Grid spacing is constant and given by $\Delta_z = z_{n+1} - z_n$ and $\Delta_y = y_{j+1} - y_j$. The rank of the resulting square matrix for which eigenvalues and eigenvectors need to be found is $5N_zN_y$. Note that the computational time to find eigenvalues scales with the cube of the rank of the matrix, i.e., with $(5N_zN_y)^3$, therefore only a rather coarse grid is feasible.

The quasigeostrophic version of the stability analysis is based on the potential vorticity equation $\partial_t q_{\mathrm{qg}} = -\mathrm{Ro}\,\underline{\nabla}\psi \cdot \nabla q_{\mathrm{qg}}$ instead of Eqs. (3)–(5), with quasigeostrophic potential vorticity $q_{\mathrm{qg}} = \nabla^2\psi + f^2/N^2\partial_{zz}\psi$ and the streamfunction ψ with $\underline{\nabla}\psi = \mathbf{u}$ and $f\partial_z\psi = b$. Defining again the jet-like mean flow with $\mathbf{u}_b(y, z)$, linearization, using the ansatz $\psi = \hat{\psi}\exp i(kx - \omega t)$ for the perturbations, and discretization in y and z leads to a similar algebraic system as before but with reduced rank of N_yN_z.

REFERENCES

Baer, F., and J. J. Tribbia, 1977: On complete filtering of gravity modes through nonlinear initialization. *Mon. Wea. Rev.*, **105**, 1536–1539, https://doi.org/10.1175/1520-0493(1977)105<1536:OCFOGM>2.0.CO;2.

Barkan, R., K. B. Winters, and J. C. McWilliams, 2017: Stimulated imbalance and the enhancement of eddy kinetic energy dissipation by internal waves. *J. Phys. Oceanogr.*, **47**, 181–198, https://doi.org/10.1175/JPO-D-16-0117.1.

Chouksey, M., 2018: Disentangling gravity waves from balanced flow. Ph.D. thesis, Universität Hamburg, 112 pp., https://doi.org/10.17617/2.3000108.

——, C. Eden, and N. Brüggemann, 2018: Internal gravity wave emission in different dynamical regimes. *J. Phys. Oceanogr.*, **48**, 1709–1730, https://doi.org/10.1175/JPO-D-17-0158.1.

Dewar, W. K., and A. M. Hogg, 2010: Topographic inviscid dissipation of balanced flow. *Ocean Modell.*, **32**, 1–13, https://doi.org/10.1016/j.ocemod.2009.03.007.

Eady, E., 1949: Long waves and cyclone waves. *Tellus*, **1**, 33–52, https://doi.org/10.3402/tellusa.v1i3.8507.

Eden, C., M. Chouksey, and D. Olbers, 2019a: Gravity wave emission by shear instability. *J. Phys. Oceanogr.*, **49**, 2393–2406, https://doi.org/10.1175/JPO-D-19-0029.1.

——, ——, and ——, 2019b: Mixed Rossby–gravity wave–wave interactions. *J. Phys. Oceanogr.*, **49**, 291–308, https://doi.org/10.1175/JPO-D-18-0074.1.

Ford, R., M. McIntyre, and W. Norton, 2000: Balance and the slow quasimanifold: Some explicit results. *J. Atmos. Sci.*, **57**, 1236–1254, https://doi.org/10.1175/1520-0469(2000)057<1236:BATSQS>2.0.CO;2.

Gertz, A., and D. N. Straub, 2009: Near-inertial oscillations and the damping of midlatitude gyres: A modeling study. *J. Phys. Oceanogr.*, **39**, 2338–2350, https://doi.org/10.1175/2009JPO4058.1.

Kafiabad, H. A., and P. Bartello, 2016: Balance dynamics in rotating stratified turbulence. *J. Fluid Mech.*, **795**, 914–949, https://doi.org/10.1017/jfm.2016.164.

——, and ——, 2018: Spontaneous imbalance in the non-hydrostatic Boussinesq equations. *J. Fluid Mech.*, **847**, 614–643, https://doi.org/10.1017/jfm.2018.338.

Machenhauer, B., 1977: On the dynamics of gravity oscillations in a shallow water model with applications to normal mode initialization. *Beitr. Phys. Atmos.*, **50**, 253–271.

Masur, G. T., and M. Oliver, 2020: Optimal balance for rotating shallow water in primitive variables. *Geophys. Astrophys. Fluid Dyn.*, **114**, 429–452, https://doi.org/10.1080/03091929.2020.1745789.

Molemaker, M. J., J. C. McWilliams, and I. Yavneh, 2005: Baroclinic instability and loss of balance. *J. Phys. Oceanogr.*, **35**, 1505–1517, https://doi.org/10.1175/JPO2770.1.

Olbers, D., J. Willebrand, and C. Eden, 2012: *Ocean Dynamics*. Springer, 726 pp.

Plougonven, R., and C. Snyder, 2007: Inertia–gravity waves spontaneously generated by jets and fronts. Part I: Different baroclinic life cycles. *J. Atmos. Sci.*, **64**, 2502–2520, https://doi.org/10.1175/JAS3953.1.

——, and F. Zhang, 2014: Internal gravity waves from atmospheric jets and fronts. *Rev. Geophys.*, **52**, 33–76, https://doi.org/10.1002/2012RG000419.

Rocha, C. B., G. L. Wagner, and W. R. Young, 2018: Stimulated generation: Extraction of energy from balanced flow by near-inertial waves. *J. Fluid Mech.*, **847**, 417–451, https://doi.org/10.1017/jfm.2018.308.

Saujani, S., and T. G. Shepherd, 2002: Comments on "Balance and the slow quasimanifold: Some explicit results." *J. Atmos. Sci.*, **59**, 2874–2877, https://doi.org/10.1175/1520-0469(2002)059<2874:COBATS>2.0.CO;2.

Savva, M. A., H. A. Kafiabad, and J. Vanneste, 2021: Inertia-gravity-wave scattering by three-dimensional geostrophic turbulence. *J. Fluid Mech.*, **916**, A6, https://doi.org/10.1017/jfm.2021.205.

Stone, P. H., 1966: On non-geostrophic baroclinic stability. *J. Atmos. Sci.*, **23**, 390–400, https://doi.org/10.1175/1520-0469(1966)023<0390:ONGBS>2.0.CO;2.

Thomsen, S., C. Eden, and L. Czeschel, 2014: Stability analysis of the Labrador Current. *J. Phys. Oceanogr.*, **44**, 445–463, https://doi.org/10.1175/JPO-D-13-0121.1.

Vanneste, J., 2013: Balance and spontaneous wave generation in geophysical flows. *Annu. Rev. Fluid Mech.*, **45**, 147–172, https://doi.org/10.1146/annurev-fluid-011212-140730.

Viúdez, Á., and D. G. Dritschel, 2004: Optimal potential vorticity balance of geophysical flows. *J. Fluid Mech.*, **521**, 343–352, https://doi.org/10.1017/S0022112004002058.

Warn, T., O. Bokhove, T. Shepherd, and G. Vallis, 1995: Rossby number expansions, slaving principles, and balance dynamics. *Quart. J. Roy. Meteor. Soc.*, **121**, 723–739, https://doi.org/10.1002/qj.49712152313.

Williams, P. D., T. W. Haine, and P. L. Read, 2008: Inertia–gravity waves emitted from balanced flow: Observations, properties, and consequences. *J. Atmos. Sci.*, **65**, 3543–3556, https://doi.org/10.1175/2008JAS2480.1.